A&A 413, 753–763 (2004)
DOI: 10.1051/0004-6361:20034060
© ESO 2003

Astronomy & Astrophysics

Band-splitting of coronal and interplanetary type II bursts

III. Physical conditions in the upper corona and interplanetary space⋆

B. Vršnak[1], J. Magdalenić[1], and P. Zlobec[2]

[1] Hvar Observatory, University of Zagreb, Kačićeva 26, HR - 10000 Zagreb, Croatia
[2] INAF – Trieste Astronomical Observatory, Via G. B. Tiepolo 11, 34131 Trieste, Italy

Received 9 July 2003 / Accepted 30 September 2003

Abstract. We analyse properties of 58 type II radio bursts recorded in the meter-to-kilometer wavelength range, focusing on episodes of band-split emission. The basic two parameters utilized are the frequency drift $D_f = \mathrm{d}f/\mathrm{d}t$ and the relative band-split $BDW = \Delta f/f$ of type II burst emission lanes. On average, in the meter-to-kilometer wavelength range D_f increases with the emission frequency as $D_f \propto f^{1.83}$, revealing that source velocities are smaller at larger heliocentric distances. The relative band-split shows a weak but statistically significant dependence on the emission frequency, $BDW \propto f^{-0.06}$, indicating an increase of BDW with the heliocentric distance.

Combining the shock velocity estimated from the frequency drift, with the Mach number inferred from the band-split, the Alfvén speed and the magnetic field in the ambient plasma can be estimated as a function of the heliocentric distance r. However, the outcome directly depends on the coronal/interplanetary density model used, which is poorly known in the upper corona and the near-Sun interplanetary space. So, we invert the problem: utilizing the results of the previous paper where it was shown that beyond the heliocentric distance of two solar radii ($r/r_\odot = R > 2$) the average magnetic field decreases approximately as $B \propto R^{-2}$, we infer the density $n(R)$ in the upper corona and near-Sun interplanetary space. The obtained empirical dependence $n(R)$ is presented in the analytical form as a four-degree polynomial of $1/R$, and is compared with some theoretical $n(R)$ models, considering also a deviation from the $B \propto 1/R^2$ scaling used. The model matches the five-fold Saito density model (representing the active region corona) with the $n \propto R^{-2}$ regime in the interplanetary space. Furthermore, it is shown that on average the magnetosonic speed attains a local minimum of $v_{\rm ms} \approx 400$ km s^{-1} around $R = 3$ and a broad local maximum of $v_{\rm ms} \approx 500$ km s^{-1} in the range $R = 4$–6, beyond which it gradually decreases to several tens km s^{-1} at 1 a.u. The local minimum becomes even deeper if the super-radial expansion of the magnetic field is taken into account.

The implications regarding the formation and evolution of shocks in the corona and upper corona are discussed in the framework of CME-piston and flare-blast scenarios. The inferred general decrease of type II burst source velocities and broadening of band-splits with distance is interpreted in terms of the deceleration of mass ejections driving the shocks in the decreasing $v_{\rm ms}$ environment.

Key words. Sun: radio radiation – MHD – shock waves – Sun: corona – interplanetary medium

1. Introduction

In the first paper of the series (Vršnak et al. 2001, hereinafter Paper I) general characteristics of the band-splitting of type II solar radio bursts (cf. Nelson & Melrose 1985) were investigated. It was shown therein that this phenomenon is not an exclusive characteristic of type II bursts recorded in the metric wavelength range, but can be found also in those recorded at deca-to-hektometer and kilometer wavelengths (hereinafter m-, DH-, and km-range, respectively). Considering only the events that in the dynamic spectrum show two "parallel" narrow-band emission lanes of synchronized intensity variations (the criteria defined in Paper I: see Sect. 2 herein), several observational and theoretical arguments were presented favouring the hypothesis that the band-split is a consequence of the plasma emission from the upstream and downstream shock regions (see also Wild & Smerd 1972; Smerd et al. 1974; Mann et al. 1995; Magdalenić et al. 2002; Vršnak et al. 2001, 2002a, 2002b). Adopting the upstream/downstream interpretation, one can use the band-split to estimate the shock amplitude, i.e., the Mach number M. On the other hand, the shock velocity can be deduced from the frequency drift. Thus, the band-split type II bursts can be used to infer the Alfvén velocity $v_{\rm A}$ and the magnetic field B, as proposed already by Smerd et al. (1974).

In the subsequent paper (Vršnak et al. 2002b, hereinafter Paper II) the radial dependencies $v_{\rm A}(r)$ and $B(r)$ were inferred

Send offprint requests to: B. Vršnak,
e-mail: bvrsnak@geodet.geof.hr

⋆ Appendices A and B are only available in electronic form at http://www.edpsciences.org

Article published by EDP Sciences and available at http://www.aanda.org or http://dx.doi.org/10.1051/0004-6361:20034060

for the coronal region utilizing a sample of type II bursts recorded at m-wavelengths. The method itself was investigated in detail to clarify how much different model-parameters influence the outcome. It was shown that the choice of the plasma-to-magnetic pressure ratio, β, and the propagation angle between the shock normal and the magnetic field, θ, influence the results much less than the choice of the model density $n(r)$ and the inclination ϕ between the density gradient and the shock normal.

After the dependence of the coronal magnetic field on the height was established, the result was combined with other relevant studies. The outcome revealed that the active region field dominates below the altitude of $H \approx 0.3$ solar radii, whereas beyond $H \approx 1$ the decrease matches very closely the relationship $B \approx 2R^{-2}$, where B is expressed in gauss and $R = r/r_\odot$ is the heliocentric distance r expressed in units of solar radius $r_\odot$, i.e., $R = H + 1$. Such a behaviour is strongly supported by polarization measurements by Habbal et al. (2001), and the relationship gives a plausible value of $B \approx 4$ nT at 1 a.u. It was also found in Paper II that the Alfvén velocity shows a local minimum of $v_A \approx 400$–500 km s^{-1} at $R \approx 2$. Then it increases towards the local maximum, which was estimated in Paper II to $v_A \approx 450$–700 km s^{-1} at $R \approx 2.5$, but it was stressed that the values defining the maximum of v_A are highly ambiguous due insufficient data coverage in the $H > 2$ range.

In this paper, the last in the series, we extend the analysis by including type II bursts recorded at DH- and km-wavelengths, being excited in the upper corona (UC) and interplanetary (IP) space. The idea is to invert the problem and to infer the poorly known behaviour of the plasma density $n(R)$ in UC and the near-Sun IP space utilizing the relationship $B \approx 2R^{-2}$ established in Paper II (see also Dulk & McLean 1978; Gopalswamy et al. 2001a). Eventually, we wish to clarify the behaviour of the Alfvén speed $v_A(R)$ and the magnetosonic speed $v_{ms}(R)$ in this range.

The first item is especially important since there is a lack of information about the $n(r)$ dependence in the near-Sun IP space. The Helios missions, (Rosenbauer et al. 1977) extended the in situ measurements down to $r \approx 0.3$ a.u. $\approx 65\ r_\odot$ (Bougeret et al. 1984a). However, the inner parts of IP space can be investigated only indirectly, e.g., utilizing measurements in the radio-range (e.g., Bougeret et al. 1984a, 1984b; Leblanc et al. 1998, and references therein). The majority of these measurements are based on the analysis of long wavelength type III bursts, and more rarely on type II bursts (e.g., Davis & Feynman 1977, see also the review by Newkirk 1967). The $n(r)$ models obtained by such studies show a great variety of slopes in UC and near-Sun IP space, frequently not compatible with the relatively well established coronal density models. Discrepancies become particularly large in matching the IP densities with the active region (AR) corona. For example, the model by Leblanc et al. (1998), which reproduces well the Helios IP-space data, gives obviously too low densities when extrapolated inwards, especially if compared with the AR-corona (see Appendix A). On the other hand, e.g., the five-fold to ten-fold Saito (1970) density model, being appropriate for the AR-corona, gives obviously too high densities when extended to the IP space.

The empirical dependence $n(R)$ obtained in this paper using the $B \propto 1/R^2$ scaling smoothly connects the AR-corona with IP space. It is presented in the analytical form as a four-degree polynomial of $1/R$ to ease comparison with other empirical results. Such an analytical form, though not physically based, also makes easier the comparison with theoretical models since they are (even in the simplest form) given as numerical solutions of different sets of equations (see, e.g., Parker 1958; Pneuman & Kopp 1971; Withbroe 1988; Coles et al. 1991; Mann et al. 2003). As an example we perform such a comparison in Sect. 4.3, where we also considered a deviation from the $B \propto 1/R^2$ scaling.

The other goal, uncovering of radial dependencies $v_{ms}(R)$ and $v_A(R)$, is essential for the comprehension of the formation and evolution of MHD shocks in the solar atmosphere (Mann et al. 1999; Gopalswamy et al. 2001a; Mann et al. 2003). A reliable $v_{ms}(R)$ model could help in resolving the question of a possibly different nature of m- and DH-type II bursts (Reiner & Kaiser 1999; Reiner et al. 2000; Gopalswamy et al. 2001a) and clarify the role of flares and CMEs in generating shocks by blast or piston mechanism (Gopalswamy et al. 1998; Cliver et al. 1999; Classen & Aurass 2002).

2. Data set and measurements

In the following we present the analysis of dynamic spectra of 40 type II bursts observed in DH-km wavelength range in the period 1991–2002, and 18 m-range type II bursts that were studied in Paper II. Twenty of DH-km type II bursts were recorded in the 1.075–13.825 MHz range by the Radio Receiver RAD1 of the Radio and Plasma Waves Instrument aboard the Wind spacecraft (Bougeret et al. 1995) and 16 in the 20–1040 kHz range by Radio Receiver RAD2[1]. The remaining 4 events were detected in the 1.25–940 kHz range by the Radio Astronomy Receiver (RAR)[2] aboard Ulysses spacecraft (Stone et al. 1992). The m-range type II bursts were recorded at the Astrophysikalisches Institut Potsdam and Culgoora Solar Observatory (for details see Paper II). The events are selected following the band-split criteria defined in Paper I: *i*) two narrow-band emission lanes (or series of patches) show a synchronized frequency time evolution, $f(t)$; *ii*) intensity fluctuations along the two lanes are similar; *iii*) the frequency ratio of the lanes is different from the harmonic/fundamental frequency ratio $f_H/f_F \approx 2$.

The band-splits and frequency drifts of type II bursts were measured applying the procedure described in details in Papers I and II. The dynamic spectrum of the band-split emission is divided into a number of roughly equidistant subintervals, depicting the times t_1 to t_N. At each of these N moments, the frequencies f_L and f_U of the emission maximum at the lower and the upper frequency branch of the band split are determined (see Figs. 1 in Papers I and II). If the measurements

[1] Kaiser, M. L.:
http://lep694.gsfc.nasa.gov/waves/waves.html
[2] MacDowall, R.:
http://urap.gsfc.nasa.gov/www/data_access.html

are performed at the harmonic emission band the frequencies are halved to get the fundamental frequency.

The number of $[f_U(t_i), f_L(t_i)]$ data pairs varied from 3 to 21 per event, depending on the duration and frequency range covered by the band split episode in a particular type II burst. From these measurements the relative band-splits $BDW(t_i)$ were determined,

$$BDW = \frac{f_U - f_L}{f_L}. \quad (1)$$

For each time interval $t_{i+1} - t_i$ the mean frequency drifts:

$$D_f(\hat{t}_i) \equiv -\left(\frac{\mathrm{d}f}{\mathrm{d}t}\right)_i = \frac{f_L(t_i) - f_L(t_{i+1})}{t_{i+1} - t_i} \quad (2)$$

and mean relative band-splits $\widehat{BDW}_i = (BDW_{i+1} + BDW_i)/2$ are evaluated, being attributed to the moment $\hat{t}_i = (t_{i+1} + t_i)/2$, and accordingly, to the frequency $\hat{f}_L = (f_{i+1} + f_i)_L/2$. In this way we obtained 243, 203, and 140 entries for D_f and BDW in the m, DH, and km range, respectively (hereinafter also denoted as coronal, UC, and IP range). The outcome is presented in Fig. 1, where the frequency drifts and band-splits are shown as a function of the frequency f_L.

Figure 1a shows the $D_f(f_L)$ dependence. The data scatter of D_f at a given frequency f is several times larger than an average error of measurements, which is roughly represented by the dimension of the dots. The power-law least squares fit gives $D_f \propto f^{1.831\pm0.009}$ with the correlation coefficient $C = 0.992$. Note however, that there is a "bump" in the DH-range $1 < f < 10$ MHz (UC region), where most of the data points are above the fitted power-law. Considering only the DH-km range, one finds $D_f \propto f^{1.990\pm0.013}$, i.e., a considerably different slope.

Figure 1b reveals that on average the relative band-split BDW increases as the observing frequency decreases. The mean values for m, DH, and km type II bursts are $\overline{BDW}_m = 0.21 \pm 0.07$, $\overline{BDW}_{DH} = 0.24 \pm 0.07$, and $\overline{BDW}_{km} = 0.30 \pm 0.09$, respectively. According to the t-test, the probability that subsamples represent underlying populations of equal mean value is smaller than 0.1% (the statistical significance of differences is larger than 99.9%).

3. The method and data reduction

3.1. Basic assumptions

The starting point of the following analysis is that the band-split depicts the plasma emission from the upstream and downstream shock region. Consequently, the relative band-split BDW is related to the density jump X at the shock front, $X = n_2/n_1 = (f_U/f_L)^2 = (1 + BDW)^2$, where n_2 and n_1 are the downstream and upstream plasma densities, respectively. The frequency of the lower frequency branch reveals the ambient plasma density, $n_1 \propto f_L^2$.

In the following we assume that the solar wind speed and density are basically isotropic, i.e., they depend only on the heliocentric distance r. In such a case, the frequency f_L is a function of the radial distance, and $f_L(t)$ reveals the change of the radial coordinate, $r(t)$, of the radio source. In other words, we presume that the frequency drift $D_f = \mathrm{d}f_L/\mathrm{d}t$ depicts the radial component of the source velocity $v_r = \mathrm{d}r/\mathrm{d}t$. In the first approximation we neglect the non-radial speed component, i.e., we assume that the type II radio sources move preferentially in the radial direction (for a discussion see Paper II, as well as Sect. 5 herein).

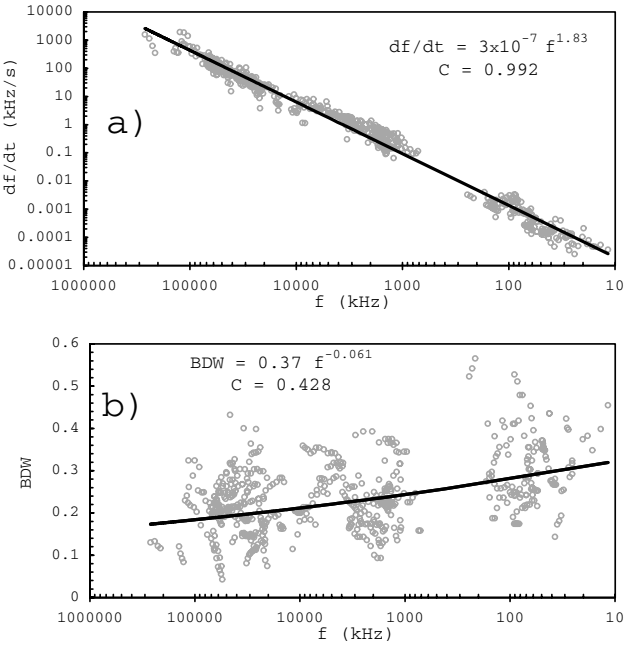

Fig. 1. Measured values of: **a)** frequency drift and **b)** relative band-split, presented as a function of the (fundamental) frequency at LFB, f_L. The x-axis scale is reversed accounting for the decrease of f with the radial distance. The power-law least squares fits and the corresponding correlation coefficients, C, are shown.

3.2. Radial distances

In the first step, the radial distances $R_i(t_i)$ are determined for each measurement $f_L(t_i)$ utilizing the two-fold Saito (1970) density model and the Leblanc et al. (1998) model (hereinafter 2S-model and L-model, respectively). At large radial distances (say, $R > 30$) the L-model is characterized by $n(R) \propto R^{-2}$ and gives a plausible value of $n \approx 7$ cm^{-3} at 1 a.u. On the other hand, the 2S-model behaves at large distances as $n(R) \propto R^{-2.5}$ and gives approximately the same density at 1 a.u. as the L-model (see Appendix A).

In the preliminary analysis by Vršnak et al. (2002a) it was shown that the L-model gives too weak magnetic field in UC, whereas the 2S-model results in too strong magnetic field for $r \to 1$ a.u. Such an outcome is a straightforward consequence of too low densities ascribed to UC by the L-model, and too steep slope of $n(r)$ in the IP space extension of the 2S-model. Since there is a lack of measurements in the (fundamental) frequency range $0.8 > f > 0.3$ MHz[3] (Fig. 1), the problem can

[3] This frequency range corresponds to the transition from RAD1 to RAD2 domain (note that some of measurements in the RAD1 domain were performed at the harmonic band). We were avoiding measurements in this range since the evaluation of D_f and BDW is ambiguous in the transition of a type II burst emission from RAD1 to RAD2 dynamical spectrum. The range corresponds roughly to $7 < R < 20$ in the L-model, and $13 < R < 30$ in the $2 \times$ S-model.

be avoided by treating the DH- and km-range subsets independently, applying the 2S-model in the $0.8 < f < 14$ MHz range, and the L-model for $f < 0.3$ MHz (as done by Vršnak et al. 2002a). Hereinafter, we call this option the 2S/L-model.

However, in the following we primarily show the results obtained by applying another density model, since it turned out that the 2S/L-model does not provide a satisfactory result (Sect. 4.1). We designed it to provide: *i*) a smooth transition of $n(r)$ from the AR-corona to the IP range; *ii*) the $B \propto R^{-2}$ relationship beyond $R \approx 2$ when applied to type II burst measurements. After combining and varying different terms in the L- and S-model we found out that the function:

$$n_{[10^8\,\mathrm{cm}^{-3}]} = \frac{15.45}{R^{16}} + \frac{3.16}{R^6} + \frac{1}{R^4} + \frac{0.0033}{R^2} \qquad (3)$$

satisfies quite well the two demands. Hereinafter, we call the dependence given by Eq. (3) the "hybrid model" (H-model). The first term on the r.h.s. of Eq. (3) is used to describe the AR-corona. It represents the five-fold Saito model at low heights, roughly corresponding to the two-fold Newkirk (1961) model, or five-fold Newkirk (1967) model (see Appendix A). The last term represents the L-model at large distances. The 2nd and 3rd term are used to match the 1st and the 4th term in such a manner that they lead to the $B \propto R^{-2}$ relationship when applied to the actual measurements. Note that the 2nd term on the r.h.s. of Eq. (3) equals the two-fold $1/R^6$ term of the Saito model, whereas the 3rd term corresponds roughly to twenty-fold $1/R^4$ term in the L-model.

In Appendix A the H-model is compared with some other empirical results, whereas in Sect. 4.3 we compare the proposed H-model with some simple theoretical density models of UC and near-Sun IP space. For example, the model by Mann et al. (2003), based on the Parker (1958) isothermal/isotropic solar wind model, is applied to the type II burst measurements and the resulting $B(R)$ dependence is then compared with the non-radial magnetic field models.

3.3. Source velocities

Heliocentric distances evaluated utilizing 2S/L-model and H-model are used to determine the radial velocities $v_i^* = \Delta r/\Delta t$. Note that the use of a lower density model generally results in smaller distances and lower speeds (data points shift to the left and downwards in the $v(R)$ graph).

The $v_i^*(\hat{R}_i)$ relationship obtained applying the H-model is shown in Fig. 2a, where $\hat{R}_i = (R_{i+1} + R_i)/2$. In Fig. 2b we present the bin-averaged values of the H-model data. The data in Fig. 2a show a weakly decreasing trend, $v^* = -2.5_{\pm 0.5} R + 800_{\pm 20}$, with a correlation coefficient $C = 0.24$. If only DH-km data are considered one finds a somewhat more pronounced decrease, $v^* = -3.4_{\pm 0.5} R + 900_{\pm 30}$, with $C = 0.38$. The power-law fit gives $v^* = 880_{\pm 30}\, R^{-0.15 \pm 0.02}$ and $v^* = 911_{\pm 80}\, R^{-0.16 \pm 0.02}$, respectively.

Let us note that the large data scatter exposed in Fig. 2a is not governed by the accuracy of measurements, but rather reflects a diversity of source speeds (see Fig. 1a). In spite of the large scatter, a variation can be noted superposed on the overall trend (the bold line in Fig. 2a). The local "maximum"

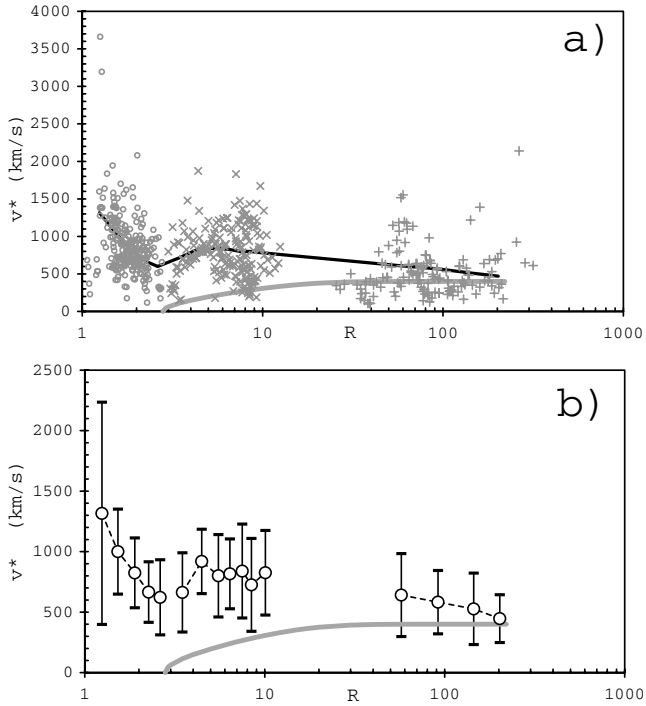

Fig. 2. Inferred radial velocities versus heliocentric distances obtained using H-model: **a)** Complete data set; **b)** Bin averaged values $\overline{v}^*(\overline{R})$ with standard deviation error bars. The empirical solar wind speed model by Sheeley et al. (1997) is shown by the thick-gray line. The thick-black line in **a)** represents the smoothed $\overline{v}^*(\overline{R})$ data from **b)**.

at $R \approx 5$ corresponds to the bump in the $D_f(f)$ curve mentioned in Sect. 2 (see Fig. 1a). The t-test statistical significance of the difference between the local minimum at $R \approx 3$ and the maximum at $R \approx 5$, estimated using the lowest and the highest bin-averaged speed in this range (Fig. 2b), is larger than $P = 99\%$.

3.4. Velocities relative to the solar wind

In UC and IP space the shocks travel in the solar wind that flows at the velocity $w(R)$. So, the shock velocity relative to the wind speed has to be estimated. For this purpose we utilize the empirical model by Sheeley et al. (1997):

$$w(R) = w_\infty \sqrt{1 - \mathrm{e}^{-(R-R_1)/R_a}} \qquad (4)$$

where $R_1 = 2.8$, $R_a = 8.1$, and w_∞ is the asymptotic value of the solar wind speed for $R \to \infty$. From Eq. (4) one finds $w = 0$ below $R \le R_1 = 2.8$, and then the speed rapidly rises to attain $w \approx w_\infty$ beyond, say, $R > 20$ (Fig. 2). $R = 2.8$ corresponds to the frequency of 9 and 13 MHz in 2S/L and H-model, respectively.

The radial velocity of the source relative to the solar wind is supposed to be $v(\hat{R}_i) = v^*(\hat{R}_i) - w(\hat{R}_i)$. However, at this point we encounter a problem: the velocities v^* show a considerable scatter and in a substantial fraction (Fig. 2) the value $v_i^*(\hat{R}_i)$ is lower than the model wind speed $w(\hat{R}_i)$. This implies $v < 0$, so that the magnetosonic speed $v_{\mathrm{ms}} = v/M$, and consequently the

magnetic field B, become negative[4]. This problem did not appear in the case of metric type II bursts (Paper II) since below $R \approx 2.8$ one can take $w = 0$. Applying the 2S/L-model with $w_\infty = 400\,\mathrm{km\,s^{-1}}$ we got two such cases (1%) in the DH-range, whereas the application of the H-model resulted in eight negative values (4%). In the IP-range 34 such measurements (31%) were obtained with both models. A larger number of the $v < 0$ data in the IP range appears because $v_i^*(R_i)$ decreases (Sect. 3.3) and $w(R)$ increases, which reduces the signal-to-noise ratio.

To avoid the problem of negative velocities, we proceed by using the bin-averaged values $\overline{v}_i^*(\overline{R})$ to evaluate $\overline{v}(\overline{R}) = \overline{v}^*(\overline{R}) - w(\overline{R})$. The bin-averaged H-model values $\overline{v}^*(\overline{R})$ that are used in the following analysis are shown in Fig. 2b together with the $w_\infty = 400\,\mathrm{km\,s^{-1}}$ solar wind speed.

The relative velocities $v_i(\hat{R}_i)$ show on average a decreasing trend, with the slope steeper than in case of $v^*(R)$. The power-law least squares fit to the bin-averaged data reads $v = 1280_{\pm 90}\,R^{-0.49\pm0.04}$ and $v = 1530_{\pm 90}\,R^{-0.54\pm0.06}$ for the complete range and the DH-km range, respectively, with the correlation coefficient of $C = 0.94$ in both options.

3.5. Shock Mach number

From the measured values of BDW we determined the corresponding shock amplitude $X = n_2/n_1 = (1 + BDW)^2$. Then, the magnetosonic Mach number M_i is evaluated from X_i using different model values of the upstream plasma-to-magnetic pressure ratio $\beta = 2\mu p/B^2$ and the angle θ between the shock normal and the upstream magnetic field (for details of the dependence $M_{\beta\theta}(X)$ see, e.g., Priest 1982, and Appendix in Paper II). The obtained $M_i(R_i)$ data are grouped into the same bins as the velocity data (Sect. 3.2) and the average values $\overline{M}(\overline{R})$ are calculated for each bin.

In Sect. 4 we show the outcome only for $\theta = 90°$ (shock normal perpendicular to the magnetic field) since it was shown in Paper II that the choice of θ does not influence the results significantly (see also Vršnak et al. 2002a): for typical band-splits $BDW = 0.2$–0.3 (Fig. 1b) the Mach number estimated by assuming the longitudinal propagation ($\theta = 0$) is $\approx 20\%$ smaller than found adopting the perpendicular propagation (see Fig. 9a in Paper II). Furthermore, it should be kept in mind that in case of the longitudinal propagation the upper limit to the value of the density jump, e.g., at $\beta = 1$, decreases to $X < 1.5$ (see Eq. (13) in Appendix of Paper II and references therein). This corresponds to $BDW < 0.22$, whereas in our sample 337 of data points (58%) had a larger band-split, reaching up to $BDW = 0.6$.

In Paper II it was shown that for $\beta < 1$ the results do not depend much on the specific value of β. However, in the corona the value of β increases with the height (cf. Gary 2001, see also Paper II) and thus its influence cannot be a priori neglected in UC and IP space. Inspecting the 1 a.u. in situ measurements one finds that apart from occasional perturbations, the value of β is generally between 0.1 and 2. So, in the analysis the values 0, 1, and 2 are applied[5].

3.6. Bin-averaging

For the coronal and UC data the bins are defined by demanding that: *i*) bins are roughly equidistant in $\log R$ scale; *ii*) each bin contains > 20 data points; *iii*) bins are sufficiently close to show the suspected v_A minimum/maximum (Paper II, Gopalswamy et al. 2001a; Mann et al. 2003). In the IP space only four bins are considered (R = 25–75, 75–125, 125–175, and 175–225) due to a lower signal-to-noise ratio, smaller amount of data, and a larger number of $v < 0$ data points.

The obtained bin-averages $\overline{v}(\overline{R}) = \overline{v}^*(\overline{R}) - w(\overline{R})$ and $\overline{M}(\overline{R})$ are used to evaluate the magnetosonic speed $\overline{v}_\mathrm{ms}(\overline{R}) = \overline{v}/\overline{M}$. From the magnetosonic speed $v_\mathrm{ms} = (v_\mathrm{A}^2 + c_S^2)^{1/2} = v_\mathrm{A}(1 + c_S^2/v_\mathrm{A}^2)^{1/2}$ one can evaluate the Alfvén speed utilizing $\overline{v}_\mathrm{A}(\overline{R}) = \overline{v}_\mathrm{ms}(1 + c_S^2/v_\mathrm{A}^2)^{-1/2} = \overline{v}_\mathrm{ms}(1 + 5\beta/6)^{-1/2}$, where we have substituted for the sound-to-Alfvén speed ratio $c_S^2/v_\mathrm{A}^2 = \gamma\beta/2$ since $c_S^2 = \gamma p/\rho$ (γ, p, and ρ are the ratio of specific heats ($\gamma = 5/3$), the gas pressure, and the mass density, respectively). Finally, the magnetic field $\overline{B}(\overline{R}) = \overline{v}_\mathrm{A}(\mu_0\rho)^{1/2}$ is calculated, substituting model densities $n(\overline{R})$ into $\rho = m_p\,n(\overline{R})$, where m_p is the proton mass.

In Sect. 4.1 we present the bin-averaged results obtained by the described procedure. However, we also applied other possible averaging sequence (e.g., starting the procedure by averaging the values of BDW, or X) and we used also the geometrical mean values. The differences in the outcome turned out to be statistically insignificant. A similar outcome is also found if firstly all individual v_ms, v_A, and B values are calculated (regardless on their sign) and only then averaged.

4. Results

4.1. Bin-averaged results

In Figs. 3a-c we show the bin-averaged values $\overline{B}(\overline{R})$, $\overline{v}_\mathrm{A}(\overline{R})$, and $\overline{v}_\mathrm{ms}(\overline{R})$. Although the evaluation follows the sequence $v_\mathrm{ms} \rightarrow v_\mathrm{A} \rightarrow B$, we present the results in the reverse order, starting by the $B(R)$ relationship in Fig. 3a to show that the H-model reproduces $B \propto R^{-2}$ dependence in the UC/IP range, whereas the 2S/L-model (shown in the inset of Fig. 3a) fails. In the UC range the power-law fit to the 2S/L-model data has the slope $B \propto R^{-1.20\pm0.07}$, i.e., the decline of the magnetic field is considerably less steep than required.

On the other hand, applying the H-model one finds $B \propto R^{-2.17\pm0.14}$ for UC range, and $B \propto R^{-1.97\pm0.05}$ when UC and IP

[4] The low v^* values are probably not due to errors in measurements: solar wind is inhomogeneous, so the density and the plasma speed can locally depart significantly from the "average" wind characteristics. The effect is twofold – local variations of the density gradient can severely affect the inferred shock velocities, and on the other hand, the wind speed can be slow locally. So, a value $v_i^*(\hat{R}_i)$ that is lower than the model value $w_i(\hat{R}_i)$ does not mean that it is lower than the true (local) value of the wind speed $w(R_i)$.

[5] The value of β is especially ambiguous in UC (Gary 2001). Note however, that taking into account the decrease of the solar wind temperature with the heliocentric distance (Priest 1982), and adopting the empirical relationship $B = 2R^{-2}$ obtained in Paper II, the value of β calculated using any of the density models presented in Appendix A and Sect. 4.3 does not exceed $\beta = 2$ in the Sun-Earth range (see also Gopalswamy et al. 2001a).

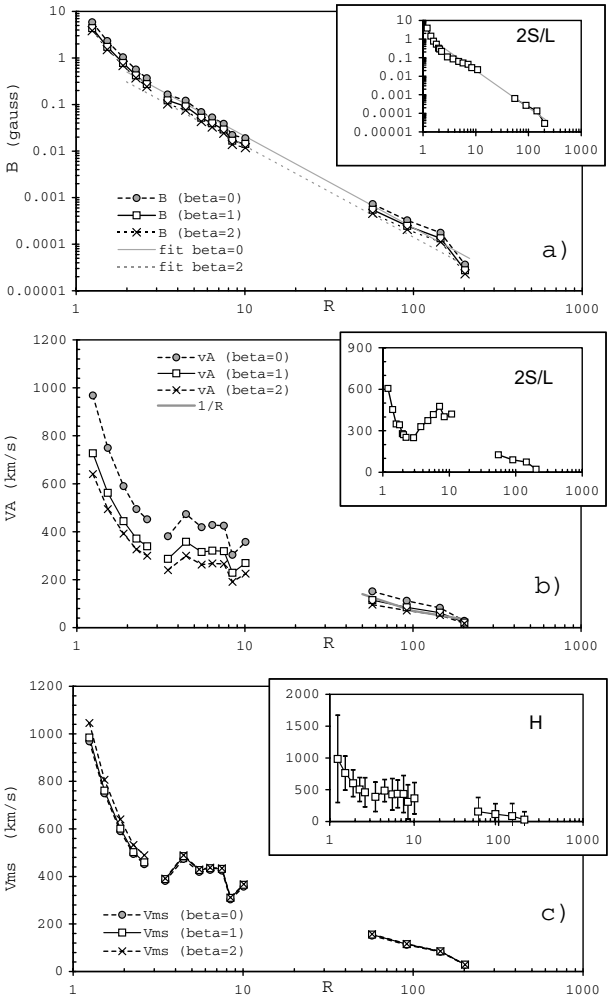

Fig. 3. Bin-averaged results for $\beta = 0$, $\beta = 1$, and $\beta = 2$ (circles, squares, and crosses, respectively) with $w_\infty = 400\,\mathrm{km\,s^{-1}}$. **a)** Magnetic field obtained utilizing H-model. The gray-full and gray-dashed lines show the power-law fits through the $\beta = 0$ and $\beta = 2$ DH-km data ($B = 1.95\,R^{-1.97}$ and $B = 1.22\,R^{-1.97}$, respectively). The results based on 2S/L-model for $\beta = 1$ are shown in the inset; gray line represents the function $B = 2 \times R^{-2}$. **b)** Alfvén speed based on H-model; gray line in the IP range represents the curve $v_\mathrm{A} = 7000R^{-1}$. In the inset the 2S/L model results are shown for $\beta = 1$. **c)** Magnetosonic speed for H-model. In the inset the H-model results for $\beta = 1$ are repeated, showing the standard deviation error bars.

data are merged. We emphasize again (see Sect. 2) that, in fact, the H-model is designed to be compatible with the $B = 2\,R^{-2}$ dependence inferred in Paper II. The gray-full and gray-dashed line in Fig. 3a show the power-law fits through the $\beta = 0$ and $\beta = 2$ DH-km data, $B = 1.95\,R^{-1.97}$ and $B = 1.22\,R^{-1.97}$, respectively, giving at 1 a.u. $B = 5$ and 3 nT. In the IP space (the four bin-averages beyond $R = 60$) the difference between the H-model and 2S/L-model results becomes negligible since in both models the R^{-2} term, adopted in H-model from the L-model, dominates.

Figures 3b and 3c show the behaviour of the Alfvén speed $\overline{v}_\mathrm{A}(\overline{R})$ and the magnetosonic speed $\overline{v}_\mathrm{ms}(\overline{R})$. The outcome for $\overline{v}_\mathrm{ms}$ is only weakly affected by the choice of β through the parametric dependence of the function $M(X)$ on the value of β (for details see Paper II). On the other hand, the inferred

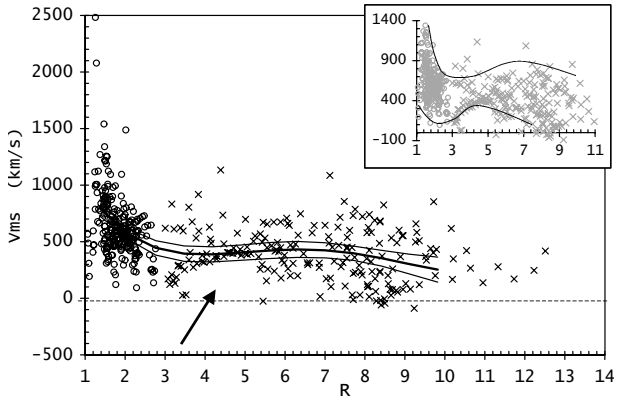

Fig. 4. Magnetosonic speeds inferred from the m and DH type II burst measurements by applying H-model (circles – m-range, crosses – DH-range). The 4th degree polynomial least squares fit is drawn (bold) together with the 99% confidence limits (thin). In the inset the same data are shown with two lines drawn provisionally to guide the eye.

Alfvén speed, which is evaluated from the magnetosonic speed, $v_\mathrm{A} = v_\mathrm{ms}(1 + 5\beta/6)^{-1/2}$, is more sensitive to the choice of β.

In the IP-range the power-law fit to the Alfvén velocity data obtained using $\beta = 1$, reads $v_\mathrm{A} = 20\,000\,R^{-1.23\pm0.38}$. Such a dependence is consistent with the $v_\mathrm{A} \propto R^{-1}$ relationship that is expected if $B \propto R^{-2}$ and $n \propto R^{-2}$. The line showing the fit cannot be resolved in Fig. 3b from the line $v_\mathrm{A} = 7000\,R^{-1}$ which gives $v_\mathrm{A} \approx 30\,\mathrm{km\,s^{-1}}$ at 1 a.u.

Figures 3b and c reveal a bump in the $v_\mathrm{A}(R)$ and $v_\mathrm{ms}(R)$ curves in the radial distance range $4 < R < 8$. Considering the potential importance of this result (Sect. 1), in the following subsection we show all $v_i^\mathrm{ms}(R_i)$ data in the coronal and UC range, in order to avoid possible artifacts caused by the sampling in the bin-averaging procedure.

4.2. Corona and upper corona – all data

The $v_i^\mathrm{ms}(\hat{R}_i)$ data shown in Fig. 4 are obtained applying the H-model, $\beta = 1$, and $w_\infty = 400\,\mathrm{km\,s^{-1}}$. Note that the x-axis scale is linear, unlike in Fig. 3 where it is logarithmic.

The large data scatter reveals a wide range of magnetosonic (and Alfvén) speeds. Yet, the distribution of data indicates a local minimum at $R \approx 3$ and a broad maximum between $R \approx 4$ and 8. It is interesting to note that there is a void of data points below $v_\mathrm{ms} \approx 400\,\mathrm{km\,s^{-1}}$ approximately in the range $3 < R < 7$ (marked by arrow; note the same void in Fig. 2a). The 4th degree polynomial least squares fit drawn in Fig. 4 together with the 99% confidence limits, shows the minimum at $R \approx 4$ and maximum at $R \approx 6$. Higher order polynomials follow a very similar behaviour in the $1.5 < R < 10$ range, only the minimum and the maximum are systematically shifted towards smaller R. For example, the 9th degree polynomial fit shows the minimum at $R \approx 3$ and maximum at $R \approx 4.5$. The correlation coefficients range from $C = 0.52$ to 0.54.

4.3. Comparison with theoretical models

After we have established the empirical $n(R)$ dependence based on the $B \propto R^{-2}$ approximation for the $R > 2$ range, it is

instructive to compare it with some theoretical solar wind models. Furthermore, it is also important to find out how much the results are affected if the deviation of the global solar magnetic field from the radial expansion is taken into account. In this section we focus primarily to the UC region since the effect should be more significant there than in the IP space where the overall situation seems to be much simpler ($B \propto R^{-2}$; see Appendix B). However, in the IP space one might consider the influence of the solar rotation, i.e., the archimedian Parker spiral, because of which the $B(R)$ slope is somewhat flatter than $B \propto R^{-2}$. If fitted by power-law, the expected average slope of the Parker spiral field from UC to 1 a.u. should be around $B \propto R^{-1.95}$, which is very close to the H-model based dependence $B \propto R^{-1.97}$ (Sect. 4.1).

Several theoretical and observational aspects complicate comparison of the presented empirical results with the solar wind models. A trivial, but technically demanding item is that even the simplest solar wind models, like the one-fluid isotropic/isothermal model by Parker (1958; see also Mann et al. 2003) provide the $n(R)$ dependence only in numerical form, i.e., they are difficult to handle in an iterative procedure like performed in previous sections, especially if free parameters of the model are to be adjusted to the observational data. Furthermore, realistic modeling of the solar wind, and consequently the comparison with the observations, are difficult for several reasons. Firstly, the solar wind energy balance, i.e., the extended heat deposition and the energy transport processes, as well as the extended momentum deposition are poorly understood (e.g., Withbroe 1988 and references therein; for a general review of the problem see Cranmer 2000). This introduces not only a number of free model-parameters, but moreover, there are different competing mechanisms and it can be only speculated which should be considered as essential and which can be neglected. Secondly, the radial dependence of the density depends significantly on the global magnetic field configuration, i.e., the change of the flux tube cross section along the field line (see, e.g., Pneuman & Kopp 1971; Withbroe 1988) which is again poorly known for the UC region. For example, most of global magnetic field models show a significant non-radial component up to several solar radii, while recent polarization measurements by Habbal et al. (2001) indicate a predominance of radial field already below $R = 2$. Furthermore, the deviation of the model-field from radial expansion is very sensitive on the heliocentric latitude (Appendix B), whereas the direction of the type II burst source propagation is not known (Sect. 3.1). Consequently, the construction of the density model that results in a certain form of $B(R)$, like performed in previous sections, is not unique (see below). So, bearing in mind also the data scatter (see Fig. 2 or 4), the observations analysed herein unfortunately can provide only a qualitative insight into the problem.

Because of the mentioned reasons, in the following we primarily focus on the simplest solar wind model (Parker 1958; Mann et al. 2003) combined with the semi-empirical dipole-quadrupole-current-sheet (DQCS) global magnetic field model by Banaszkiewicz et al. (1998; for details see Appendix B). Furthermore, since below $R \approx 2$ the magnetic filed is locally dominated by the active region field (see Fig. 7b in Paper II; for older measurements see Newkirk 1967), the comparison with the theoretical global models becomes reasonable only beyond $R \approx 2$.

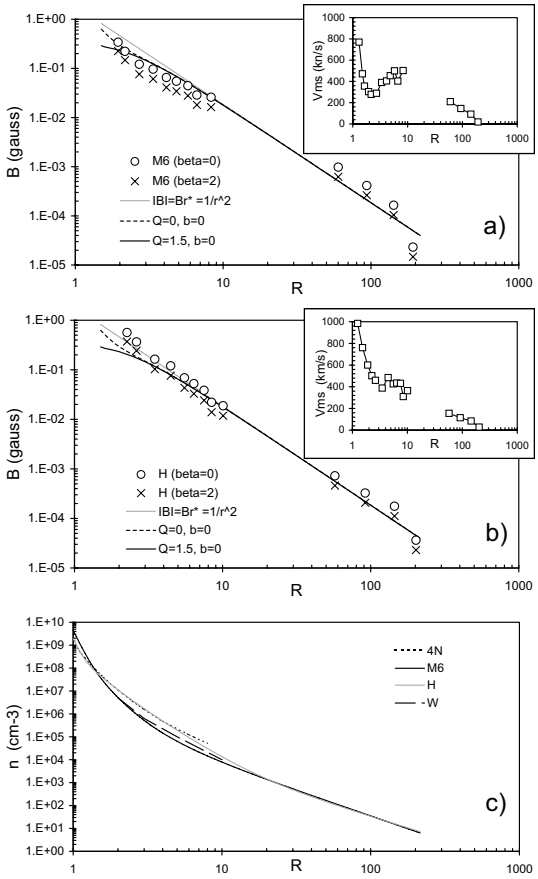

Fig. 5. $B(R)$ dependence beyond $R = 2$ based on: **a)** Mann et al. (2003) density model; **b)** H-model. Circles show results for $\beta = 0$ and crosses for $\beta = 2$. The gray-bold line represents $B \propto R^{-2}$, whereas full and dashed black curves represent the equatorial dipole-current-sheet field and dipole-quadrupole-current-sheet field, after the model by Banaszkiewicz et al. (1998). The field strength is normalized to 4 nT at 1 a.u., and we take $a = 1.538$ and $K = 1$ (for details see Appendix B). In the insets the dependencies $v_{\rm ms}(R)$ are shown. **c)** Comparison of H-model density (gray-bold line) with the models by Mann et al. (2003), Withbroe (1988), and four-fold Newkirk (1967) model (full (M6), long-dashed (W), and dotted (4N) black lines, respectively).

In Fig. 5a we show the magnetic field inferred from the type II burst data by applying the isotropic and isothermal ($T = 10^6$ K) solar wind model discussed by Mann et al. (2003; hereinafter M6-model). The outcome is compared with the magnetic field strengths in the equatorial region in the DQCS-model and dipole-current-sheet approximation ($Q = 1.5$ and $Q = 0$, respectively; for details see Appendix B).[6] The form of the inferred $B(R)$ relationship in the UC range reminds to the outcome for the 2S/L-model shown in Fig. 3a (compare also the insets in Figs. 3b and 5a), i.e., the slope of $B(R)$ is significantly flatter than the $B \propto R^{-2}$ dependence. Comparing the inferred field with the model-field one finds that slope of

[6] Note that in the equatorial region the magnetic field reconnection can play a significant role and dynamically modify the basic field (see, e.g., Wu et al. 2000; Endeve et al. 2003), further complicating the situation.

the inferred field qualitatively behaves like the DQCS-field (see Appendix B). Yet, the UC field is systematically weaker than expected from DQCS-model. Thus the M6-model densities should be increased in the UC range, meaning that the model-temperature (the only free parameter in the model) should be somewhat lower. So, M6-model can be considered as the lower limit to the densities in the UC range. (Note that applying a lower model-temperature one gets considerably overestimated densities below $R \approx 2$, whereas in the IP range the slope of the $n(R)$ dependence becomes significantly steeper than $n \propto R^{-2}$.)

In Fig. 5b we compare the $B(R)$ dependence based on the H-model with DQCS-field. One finds that although the inferred field generally follows the $B \propto R^{-2}$ dependence, the distribution of points is again suggestive of DQCS-field behaviour. The two data-points at lowest R could be reflecting the influence of active region fields. Another possibility is that the contribution of the quadrupolar field is small (see the dashed line, $Q = 0$). Yet, bearing in mind the data scatter (and other drawbacks itemized in Sect. 5.2), one has to consider the deviation from $B \propto R^{-2}$ as statistically insignificant (see, e.g., the last three points in $R = 7{-}10$ range). Moreover, we emphasize again the measurements by Habbal et al. (2001) which indicate predominance of the radial field in the corona. If nevertheless one adopts that the effects of DQCS-field dominate along the type II burst trajectory, the H-model densities should be considered as the upper limit for the densities in the UC range (values of B are systematically larger than in the DQCS-model).

In Fig. 5c we compare the M6-model and H-model $n(R)$ dependencies, presumably representing the lower and upper limit for $n(R)$ in the UC range. In the range $R = 2{-}10$ the densities differ by factor 2–4, which is considerably less than differences between various empirical models (Appendix A). In addition we show (long-dash curve denoted as "W") the outcome of the *quiet region* solar wind model by Withbroe (1988) for the conductive loss at the chromospheric upper boundary of $F_c = 10^{5.5}\,\mathrm{erg\,cm^{-2}\,s^{-1}}$ (dot-dash curve in Fig. 4 therein). The location of W-curve between H and M6 curves, indicates that the Withbroe's model can account for the observations, however demanding a relatively high conductive losses, inclining towards $F_c = 10^6\,\mathrm{erg\,cm^{-2}\,s^{-1}}$. Indeed, the conductive loss in the active region corona could be larger than in quiet regions due to larger coronal temperatures. Finally, in Fig. 5c we also show (dotted line, 4N) the four-fold density model by Newkirk (1967), usually considered as a good representative of the active region corona. One finds a very close agreement between 4N-model and H-model densities in the range $R < 10$.

5. Discussion

5.1. Magnetosonic speed and evolution of shocks

Let us first briefly summarize and discuss the results that are not significantly affected by the applied procedure and the model parameters used:

- Frequency drifts D_f of type II bursts decrease from the corona to 1 a.u., following the power-law relationship $D_f \propto f^{1.83\pm0.01}$, or $D_f \propto f^{1.99\pm0.01}$ if only the UC/IP range is considered;
- Relative band-splits of type II bursts on average increase ($BDW \propto f^{-0.061\pm0.005}$);
- Source radial velocities generally decrease in the IP space, $v^* \propto R^{-0.16\pm0.02}$, but in UC show a local minimum and maximum;
- Source velocities relative to the solar wind on average decrease as (roughly) $v \propto R^{-1/2}$;
- Magnetosonic speed shows a local minimum at $R \approx 3$ and maximum at $R \approx 4{-}6$.

Note that relationships in the first two items are entirely model-independent. The other three items depend on the choice of the $n(R)$ model only quantitatively: general behaviour remains similar for any monotonously decreasing Sun-Earth $n(R)$ model.

Taking approximately $n \propto r^{-\alpha}$ and assuming $v^* = \mathrm{d}r/\mathrm{d}t \approx const.$, one finds $D_f = \mathrm{d}f/\mathrm{d}t \propto f^{1+2/\alpha}$ since $f \propto \sqrt{n}$. Comparing the exponent $1+2/\alpha$ with the measured exponent b of the $D_f \propto f^b$ dependence given in the first item, the slope in the $n \propto r^{-\alpha}$ dependence can be estimated as $\alpha = 2/(b-1)$. Specifically, one finds that the density decreases as $n \propto R^{-2.02}$ in the UC/IP range ($b = 1.99$, see Sect. 2), or $n \propto R^{-2.41}$ if all the data are considered ($b = 1.83$). These slopes are slightly less steep than found in previous analogous studies (Bougeret et al. 1984a). Taking into account that on average the velocities in the UC/IP space decrease, and approximating $v^* \propto R^{-\gamma}$ (3rd item) one finds $\alpha = 2(1+\gamma)/(b-1)$, i.e., $n \propto R^{-2.3}$ and $n \propto R^{-2.8}$, respectively.

The existence of the local minimum and maximum of the magnetosonic speed (last item) could be in fact deduced *ad hoc* from the presence of the local minimum and maximum in the $v^*(R)$ graph of source velocities (3rd item, Fig. 2) – it is enough to suppose that the shock amplitude (Mach number) does not change significantly in this range. Note that this argument is independent of the upstream/downstream interpretation of the band-split. Finally, we emphasize that the bump in the $v_{\mathrm{ms}}(R)$ dependence is found to be present whatever density model we used. In fact, its amplitude is the smallest for the H-model and the $B \propto R^{-2}$ assumption – the local minimum at $R \approx 3$ becomes deeper when the super-radial expansion of the field is considered (see the inset in Fig. 5a).

The increase of BDW and the decrease of v (2nd and 4th item, respectively) can be explained straightforwardly by adopting that the UC/IP type II bursts are excited at the CME-driven shocks. In the UC and IP space CMEs decelerate due to the drag force (Gopalswamy et al. 2001b; Vršnak 2001; Vršnak & Gopalswamy 2002) which is especially prominent in type II burst associated CMEs (Gopalswamy et al. 2001c). Consequently, the source velocities of type II bursts show on average a decreasing trend in the IP space. On the other hand, the magnetosonic speed in the IP space decreases too, and if the deceleration rate $\mathrm{d}v/\mathrm{d}R$ of the driver is smaller than $\mathrm{d}v_{\mathrm{ms}}/\mathrm{d}R$, the ratio $M = v/v_{\mathrm{ms}}$ increases. Since the Mach number increases, the shock amplitude (density jump) increases too, resulting in the increasing trend of band-splits.

At this point it is appropriate to note that the $v \propto R^{-1/2}$ relationship (4th item) was recognized in a number of case studies of IP shocks (see, e.g., Smart & Shea 1985, or Pintér & Dryer 1990 and references therein) after the "flare-driven" phase. Such a behaviour was interpreted as a consequence of self-similar evolution of the shock (Smart & Shea 1985) following the famous consideration of nuclear bomb explosion by Sedov (1959); see also Landau & Lifshitz (1987). Note however, two drawbacks of such an interpretation. Firstly, the $v \propto R^{-1/2}$ scaling holds for the plane geometry (in the spherical case the exponent is $-3/2$, Sedov 1959). Secondly, it would be more appropriate to consider CME as an "explosion" which initially acts as the cylindrical/spherical piston driving the shock (Sedov 1959). After the cessation of the CME-propelling force, i.e., after the energy input ends (corresponding to the end of the type IV radio burst phase in the flare-scenario by Pintér & Dryer 1990) the shock would propagate as a freely moving, shocked spherical simple-wave (Landau & Lifshitz 1987). In the uniform gas its amplitude would decrease as $1/R \log R$ (Landau & Lifshitz 1987), which however, should be considerably modified in the decreasing density magnetoplasma.

The behaviour of the magnetosonic speed in the AR-corona that is described in the last item was anticipated by Gopalswamy et al. (2001a) and Mann et al. (2003). Such a behaviour has important implications for the formation and evolution of shocks in the solar corona. For example, either a flare generated blast, or the perturbation ahead of CME, is most likely to steepen into the shock in the region of decreasing magnetosonic speed and the region of its minimum (for a discussion see Vršnak & Lulić 2000a). On the other hand, it is more difficult to create a shock in the region of increasing magnetosonic speed and its maximum. Moreover, the flare ignited shocks, created out of large amplitude simple waves (Vršnak & Lulić 2000b) are supposed to cease in the region of $v_{\rm ms}$ maximum.

Finally, it should be emphasized that the presented results are based on the statistical consideration, so in an individual AR the "bump" in $v_{\rm ms}$ and $v_{\rm A}$ curve can be narrower. It is reasonable to assume that the height at which the maximum appears varies from one AR to another: the superposition of $v_{\rm A}(R)$ curves smears the minimum and maximum in the "average" curve.

5.2. Density and magnetic field from AR-corona to IP space

Another interesting aspect of the presented analysis is that the density behaviour $n(R)$ can be inferred by presuming the $B(R)$ dependence. It turned out that the density 2S/L-model is not compatible with the $B \propto R^{-2}$ dependence in the UC region (inset in Fig. 3a). For this reason we designed a density model which smoothly connects the AR-corona with the IP space and is consistent with the $B \propto R^{-2}$ approximation. At metric wavelengths the model corresponds to the five-fold Saito (1970) model (appropriate for the AR-corona), whereas in the IP space behaves like the Leblanc et al. (1998) model which reproduces the in situ Helios measurements.

Although the proposed density model apparently fits the observations, one must bear in mind several important constraints:

1. Although it was shown in Paper II that the magnetic field starts to decrease as $B = 2R^{-2}$ beyond $R > 2$ (as noted already by Dulk & McLean 1978; see also Gopalswamy et al. 2001a; Habbal 2001), giving a plausible value $B \approx 4$ nT at 1 a.u., it is not *necessarily* true that the R^{-2} dependence strictly holds across the whole distance range, especially in the UC region (see Appendix B).
2. The type II emission could be excited preferably at locations of some specific physical condition (as could be suspected due to the patchy character of the emission – see Paper I), so the obtained parameters might not be appropriate to represent an "average state" of the UC/IP space.
3. Sources of type II bursts possibly propagate in directions significantly inclined to the density gradient (the angle ϕ): if so, the inferred velocity v^* is lower than the shock velocity. Consequently, a higher density model has to be applied to get a "proper" value for B, i.e., the H-model densities might be overestimated. Moreover, if for some reason ϕ systematically changes along R it will affect the deduced slope of $n(R)$.
4. The results depend on the solar wind speed model, primarily through the choice of the asymptotic speed w_∞, or analogously through the angle between the radio source motion and the wind direction (presumably equal to ϕ). For example, if the wind speed is underestimated, the inferred relative velocity $v = v^* - w$ is overestimated, and in such a case the H-model densities are underestimated.
5. The value of β becomes ambiguous in UC and the values of β might be larger than considered. However, large values of β would demand for unreasonably high model-densities, which would be incompatible with the AR-corona densities and the $R > 60$ Helios measurements (in addition, see the footnote 5 in Sect. 3.5). Note also that this item does not affect qualitatively the results summarized in Sect. 5.1.
6. Our data set includes measurements in different phases of the solar cycle which additionally increases the scatter in the data since the average density varies considerably with the solar cycle (see, e.g., Bougeret et al. 1984a).

Bearing in mind the data scatter and the items 1-6, it can be concluded that it is relatively irrelevant which value θ is chosen in constructing the density model. Furthermore, the effect of the inclination ϕ of the source velocity from the radial density gradient becomes important for, say, $\phi > 30°$. At this value the real speed is 15% larger than inferred assuming $\phi = 0$. So, the inclination ϕ is also not likely to influence the results crucially (for a discussion see Paper II and Vršnak et al. 2002a). Similarly, the details of the bin averaging procedure (Sect. 3.6), or details of the solar wind model used[7], do not affect the results significantly.

[7] A very similar outcome is found utilizing the isotropic wind model that is based on the continuity equation applied to the 2S/L- and H-model ($nwR^2 = const.$, see Vršnak et al 2002a).

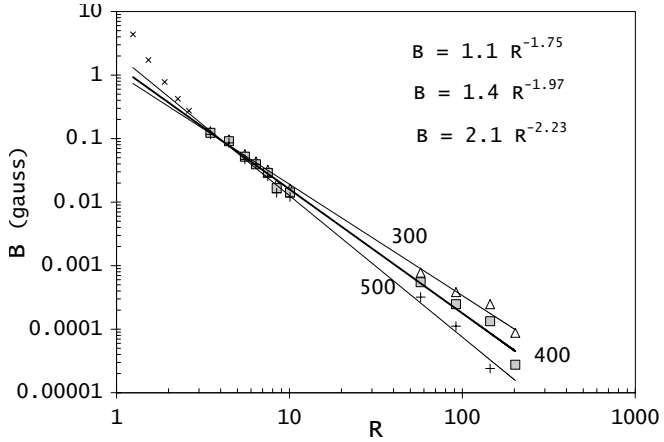

Fig. 6. $B(R)$ relationship obtained using H-model with $\beta = 1$ and $w_\infty = 300$, 400, and 500 km s^{-1} (triangles, squares, and pluses, respectively). The power-law function is fitted only to UC/IP-range data. The coronal data are depicted by crosses.

On the other hand, the parameter that directly affects the result is the asymptotic value of the solar wind speed w_∞ (item 4). For this reason we checked also the outcome for $w_\infty = 300$ and 500 km s^{-1} (Fig. 6). In the case of $w_\infty = 500$ km s^{-1} the mean relative speed $\overline{v} = \overline{v}^* - w$ becomes negative in the last IP-range bin, leading to $\overline{B} < 0$. To avoid such a non-physical result, one would have to redesign H-model in a manner that is incompatible with Helios data and 1 a.u. measurements. Even neglecting the last bin-averaged value one gets $B \propto R^{-2.23}$ for the UC/IP range, i.e., a too steep slope.

Taking $w_\infty = 300$ km s^{-1} the number of individual $v < 0$ data is reduced for H-model to only two in UC (1%) and to 17 (15%) in the IP range. The $B(R)$ dependence in UC/IP space becomes $B \propto R^{-1.75}$: to correct this, the H-model should be modified in UC-range by increasing the density there. However, with $w_\infty = 300$ km s^{-1} one also finds that $v_A \propto R^{-0.64}$ for the IP-range data. Such a slope is not steep enough since it deviates significantly from the $v_A \propto R^{-1}$ relationship that is expected if $B \propto R^{-2}$ and $n \propto R^{-2}$ (results of the Paper II and the Helios measurements, respectively). This indicates that $w_\infty = 400$ km s^{-1} is a better choice. A good match of the $w_\infty = 400$ km s^{-1} model, being usually referred as an average wind speed, indicates that sources of type II bursts, in a statistical sense, move more or less radially.

6. Conclusion

The presented analysis shows that it is possible to construct a density model that smoothly connects the active region corona with the IP space and is consistent with the $B \propto R^{-2}$ decrease of the magnetic field when applied to type II bursts recorded beyond $R \approx 2$. Taking into account the super-radial expansion of the magnetic field, one finds that the isothermal density model by Mann et al. (2003) can be considered as a lower limit of the density in UC and near-Sun IP space, whereas the H-model given by Eq. (3) is closer to an upper limit. A high-conductive-loss option of the model by Withbroe (1988) seems to provide the most realistic representation of this range. In the $R > 60$ range, the model by Mann et al. (2003) and H-model converge and are consistent with the Helios in situ measurements.

The analysis reveals a complex dependence of the magnetosonic and Alfvén speeds in UC. Regardless on the density model used, the magnetosonic speed attains a local minimum around $R \approx 3$ ($v_{ms}^{min} \approx 200$–400 km s^{-1}, depending on the density model) and a broad local maximum of $v_{ms} \approx 500$ km s^{-1} in the range $R \approx 4$–6. Such a dependence has direct consequences for the formation and evolution of shocks in the solar corona and upper corona. Finally, a monotonous decrease of the magnetosonic speed beyond $R \approx 10$ explains the statistical trend of decreasing shock velocities and increasing shock amplitudes in the IP space.

Acknowledgements. We are grateful to the Ulysses and Waves/Wind teams for operating the instruments and performing the basic data reduction, and especially for the open data policy. We would like to thank the referee for constructive suggestions.

References

Banaszkiewicz, M., Axford, W. I., & McKenzie, J. F. 1998, A&A, 337, 940
Bougeret, J.-L., King, J. H., & Schwenn, R. 1984a, Sol. Phys., 90, 401
Bougeret, J.-L., Feinberg, J., & Stone, R. G. 1984b, A&A, 141, 17
Bougeret, J.-L., Kaiser, M. L., Kellogg, P. J., et al. 1995, Space Sci. Rev., 71, 231
Classen, H. T., & Aurass, H. 2002, A&A, 384, 1098
Cliver, E. W., Webb, D. F., & Howard, R. A. 1999, Sol. Phys., 187, 89
Coles, W. A., Esser, R., Lovhaug, U.-P., & Markkanen, J. 1991, J. Geophys. Res., 96, 13849
Cranmer, S. R. 2000, Coronal Holes in Encyclopedia of Astronomy, ed. P. Murdin (Institute of Physics Publishing, Grove's Dictionaries Inc., New York), 1, 496
Davis, W. D., & Feynman, J. 1977, J. Geophys. Res., 82, 4699
Dulk, G. A., & McLean, D. J. 1978, Sol. Phys., 57, 279
Endeve, E., Leer, E., & Holzer, T. E. 2003, ApJ, 589, 1040
Fainberg, J., & Stone, R. G. 1971, Sol. Phys., 17, 392
Frazin, R. A., & Janzen, P. 2002, ApJ, 570, 408
Gary, G. A. 2001, Sol. Phys., 203, 71
Gopalswamy, N., Kaiser, M. L., Lepping, R. P., et al. 1998, J. Geophys. Res., 103, 307
Gopalswamy, N., Lara, A., Kaiser, M. L., & Bougeret, J.-L. 2001a, J. Geophys. Res., 106, 25261
Gopalswamy, N., Lara, A., Yashiro, S., Kaiser, M. L., & Howard, R. A. 2001b, J. Geophys. Res., 106, 29207
Gopalswamy, N., Yashiro, S., Kaiser, M. L., Howard, R. A., & Bougeret, J.-L. 2001c, J. Geophys. Res., 106, 29219
Habbal, S. R., Woo, R., & Arnaud, J. 2001, ApJ, 558, 852
Landau, L. D., & Lifshitz, E. M. 1987, Fluid Mechanics, 2nd edn. (Oxford: Pergamon Press)
Leblanc, Y., Dulk, G. A., & Bougeret, J.-L. 1998, Sol. Phys., 183, 165
Magdalenić, J., Vršnak, B., & Aurass, H. 2002, Proc. 10th European Solar Physics Meeting, Solar Variability: From Core to Outer Frontiers, ESA SP-506, 335
Mann, G., Classen, T., & Aurass, H. 1995, A&A, 295, 775
Mann, G., Aurass, H., Klassen, A., Estel, C., & Thompson, B. J. 1999, ESA SP-446, 477
Mann, G., Klassen, A., Aurass, H., & Classen, H.-T. 2003, A&A, 400, 329
Nelson, G. S., & Melrose, D. B. 1985, in Solar radiophysics, ed. D. J. McLean, & N. R. Labrum (Cambridge: Cambridge Univ. Press), 333

Newkirk, G. Jr. 1961, ApJ, 133, 983
Newkirk, G. Jr. 1967, ARA&A, 5, 213
Parker, E. N. 1958, ApJ, 128, 664
Pintér, Š., & Dryer, M. 1990, Bull. Astron. Inst. Czechosl., 41, 137
Pneuman, G. W., & Kopp, R. A. 1971, Sol. Phys., 18, 258
Priest, E. R. 1982, Sol. Magnetohydrodyn. (Dordrecht: Reidel)
Reiner, M. J., & Kaiser, M. L. 1999, J. Geophys. Res., 104, 16979
Reiner, M. J., Kaiser, M. L., Plunkett, S. P., Prestage, N. P., & Manning, R. 2000, ApJ, 529, L53
Rosenbauer, H., Schwenn, R., Marsch, E., et al. 1977, J. Geophys. Res., 42, 561
Saito, K. 1970, Ann. Tokyo Astr. Obs, 12, 53
Sedov, L. I. 1959, Similarity and Dimensional Methods in Mechanics, Academic, New York
Sheeley, N. R. Jr., Wang, Y.-M., Hawley, S. H., et al. 1997, ApJ, 484, 472
Smart, D. F., & Shea, M. A. 1985, J. Geophys. Res., 90, 183
Smerd, S. F., Sheridan, K. V., & Stewart, R. T. 1974, in IAU Symp., 57, ed. G. A. Newkirk, 389
Stone, R. G., Bougeret, J. L., Caldwell, J., et al. 1992, A&AS, 92, 291
Strachan, L., Suleiman, R., Panasyuk, A. V., Biesecker, D. A., & Kohl, J. L. 2002, ApJ, 571, 1008
Vršnak, B. 2001, Sol. Phys., 202, 173
Vršnak, B., & Lulić, S. 2000a, Sol. Phys., 196, 157
Vršnak, B., & Lulić, S. 2000b, Sol. Phys., 196, 181
Vršnak, B., & Gopalswamy, N. 2002, J. Geophys. Res., 107, 10.1029/2001AJ000120
Vršnak, B., Aurass, H., Magdalenić, J., & Gopalswamy, N. 2001, A&A, 377, 321
Vršnak, B., Magdalenić, J., Aurass, H., & Mann, G. 2002a, Proc.10th. European Solar Physics Meeting, Solar Variability: From Core to Outer Frontiers, ESA SP-506, 409
Vršnak, B., Aurass, H., Magdalenić, J., & Mann, G. 2002b, A&A, 396, 673
Wild, J. P., & Smerd, S. F. 1972, ARA&A, 10, 159
Withbroe, G. L. 1988, ApJ, 325, 442
Wu, S. T., Wang, A. H., Plunkett, S. P., & Michels, D. J. 2000, ApJ, 545, 1101